



Universiteit  
Leiden  
The Netherlands

## **Optoplasmonic detection of single particles and molecules in motion**

Asgari, N.

### **Citation**

Asgari, N. (2023, November 28). *Optoplasmonic detection of single particles and molecules in motion*. *Casimir PhD Series*. Retrieved from <https://hdl.handle.net/1887/3665158>

Version: Publisher's Version

License: [Licence agreement concerning inclusion of doctoral thesis in the Institutional Repository of the University of Leiden](#)

Downloaded from: <https://hdl.handle.net/1887/3665158>

**Note:** To cite this publication please use the final published version (if applicable).

## 2

# Photothermal Spectro-Microscopy as Benchmark for Optoplasmonic Bio-Detection

*Optoplasmonic bio-detection assays commonly probe the response of plasmonic nanostructures to changes in their dielectric environment. The accurate detection of nanoscale entities such as virus particles, micelles and proteins requires optimization of multiple experimental parameters. Performing such optimization directly via analyte recognition is often not desirable or feasible, especially if the nanostructures exhibit limited numbers of analyte binding sites and if binding is irreversible. Here we introduce photothermal spectro-microscopy as a benchmarking tool for the characterization and optimization of optoplasmonic detection assays.*

---

<sup>1</sup>Baaske, M. D., Asgari, N., Spaeth, P., Adhikari, S., Punj, D., & Orrit, M. (2021). Photothermal spectro-microscopy as benchmark for optoplasmonic bio-detection assays. *The Journal of Physical Chemistry C*, 125(45), 25087-25093.

## 2.1 Introduction

Individual (bio)molecules can be detected optically through their fluorescence [65], absorption [61], or mere refraction [66]. Opto-plasmonic methods, which harness strong nearfields around plasmonic metal nanostructures to enhance the sensitivity and selectivity of optical detection, have evolved over the past decade into powerful tools for biomolecular recognition. Dedicated versions of these methods now enable the detection of a wide range of molecules and nanoparticles, on a single-object basis [28, 31, 67–69]. Sensitive refractometric sensors such as optical microresonators also provide powerful platforms for molecular recognition [70], especially in combination with plasmonic particles [21, 32–34, 71]. At the same time novel microscopic methods make use of plasmonic particles as photostable labels [72, 73] and combine them with optical, electromagnetic, or electric devices for trapping and manipulation of sensor particles or even of the molecules themselves [74, 75]. In the following we will exclusively focus on optoplasmonic assays that facilitate analyte recognition via observation of a plasmonic nanostructure’s response to (single) analytes perturbing its dielectric environment. The volume in which such perturbations are recognizable is defined by the extent of the structures’ enhanced near-field and is limited to distances on the order of 10 nm away from the structures’ surface. Optoplasmonic assays commonly employ specific receptor molecules to bind analytes and to facilitate their detection. These receptors fulfill a dual purpose: (i) They immobilize the analytes inside the detection volume and, thus, provide for long enough integration times required for the detection of the target. (ii) They provide target specificity, as they ideally form sufficiently strong binding exclusively with the targeted molecules. As a consequence, the sensitivity of refractometric optoplasmonic assays depends on two separate factors: (i) The properties of the chemical interface, that is, receptor density, accessibility, and quality; (ii) The properties of the plasmonic structure and the optical interface, that is, spectral quality, spectral position of plasmonic features, structure quality, polarization states, wavelength range, desired bandwidth, type of illumination (widefield or confocal), and the detection electronics. To allow for the consecutive optimization of aspects (i) and (ii), it is desirable to characterize these aspects separately and independently. Here, we show in the example of gold nanorods that photothermal spectro-microscopy provides such a characterization method for plasmonic structures, that is, for aspect (ii).

## 2.2 Methods

**Slide Preparation.** Gold nanorods (GNRs) were purchased from Nanopartz. NRs were sonicated for 20 min and then spincoated onto microscope slides. Next the glass slides were deposited in a UV-ozone cleaner for 60 min in order to remove residual CTAB and consecutively rinsed with water. Measurements were then performed in glass chambers made from BK-7 and pressed against the slides. Chemicals were purchased from Sigma-Aldrich.

**Optical Setup** We used the custom-made confocal setup depicted in figure. 2.1a. Its components are: Objective: Olympus UPLFLN100XOP; Tube lens: Olympus Super Wide Tube Lens Unit; Lasers: Toptica DL pro 785 nm and Cobolt Samba 532 nm; APD: Thorlabs APD430A/M; 10:90 Beamsplitter BSN11 (Thorlabs); Glan-Thompson Polarizer GTH10M-B (Thorlabs); Piezo Translator P-561.3CD (Physik Instrumente GmbH & Co KG); White-light source: EQ-99XFC (Energetiq); Spectrometer: QE-65000 (Ocean Optics); Reference Photodiodes 1 and 2: PDA36A2 (Thorlabs) and HCA-S-200 M (Femto); EOM: Amplitude Modulator AM532 (Jenoptik); AOM: MT110-A1-IR (AA Opto-Electronic); Achromatic  $\lambda/2$ -plate: RAC 4.2.10 (B. Halle); Notch Filter: ZET532NF (Chroma). Data was recorded via an Oscilloscope (Wave-Surfer 24MXs-B, Teledyne Lecroy).

## 2.3 Results and Discussion

Photothermal (PT) microscopy detects a change of optical properties following the absorption of light by an analyte [76]. The dissipation of the absorbed power into the surrounding medium induces a temperature gradient, which modifies the optical properties both of the absorbing objects and of the medium. The associated change of the medium's refractive index notably leads to the formation of a thermal lens [64, 77]. Heating-induced changes in the optical properties lead to changes in the scattered light, which are detected as intensity changes of a probe beam illuminating the sample. As these changes are very small, their detection is facilitated if the heating beam's intensity is modulated at a fixed frequency, enabling subsequent phase-sensitive demodulation via a lock-in amplifier which rejects most white and  $1/f$  noise. Commonly, the probe beam is used off-resonance so that high probe powers can be used [64, 78]. Here, we deviate from this scheme by probing gold nanorods at wavelengths close to their localized surface plasmon resonance (LSPR), as we are interested in probing their response to heat-induced refractive index changes. We do this with the confocal

microscopy setup shown in figure. 2.1.

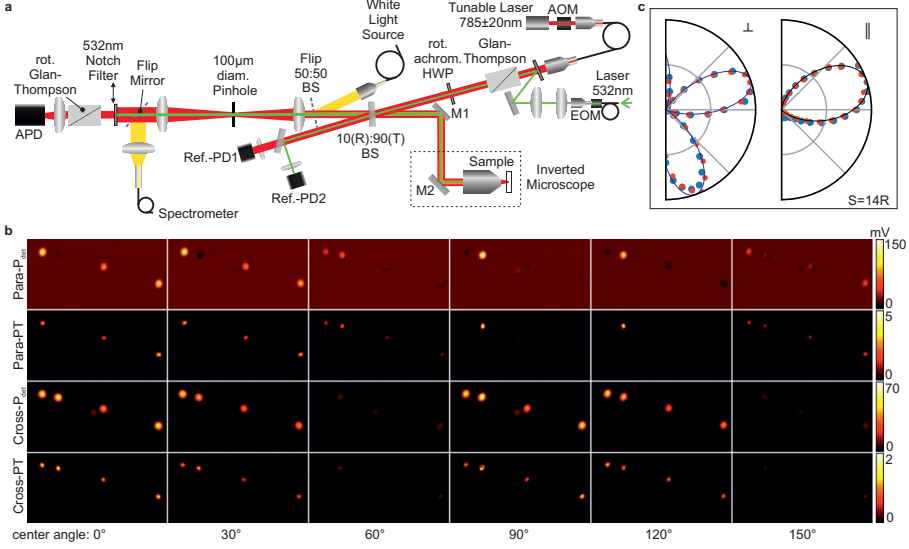


**Figure 2.1:** **a)** Confocal microscopy setup used for the combined positional, orientational, spectral, and photothermal characterization of single gold nanorods. **b)** Confocal scanning images of  $P_{det}$  and  $\Delta P_{PT}$  measured on the same sample area and obtained with crossed (Cross) and parallel (Para) polarizers at different center angles. **c)** Angle scans of the same GNR with crossed (left) and parallel (right) polarizers: Blue (red) dots mark the  $P_{det}$  ( $\Delta P_{PT}$ ) values normalized to their corresponding maximum. Solid lines indicate fits by the theoretical functions.

We detect changes in the power  $P_{det}$  of the detected probe light, which results from the interference between scattered  $E_s \propto \sqrt{S}e^{-i\theta}$  and reflected  $E_r \propto \sqrt{R}e^{-i\gamma}$  electric fields:

$$P_{det} \propto (E_s + E_r)(E_s + E_r)^* \propto R + 2\eta\sqrt{SR}\cos\phi + S, \quad (2.1)$$

where  $*$  denotes the complex conjugate, and  $R$  and  $S$  are the effective reflection coefficient and scattering cross section, respectively. Further,  $\phi = \theta - \gamma$  denotes the phase difference between the reflected and the scattered field, where  $\gamma$  is the Gouy phase and  $\theta$  is the phase difference between incident and scattered field. Both  $S$  and  $\theta$  depend on the frequency detuning of the probe laser's frequency  $\nu$  with respect to the resonance frequency of the GNR's LSPR frequency,  $\nu_{LSPR}$ . The factor  $\eta$  denotes the mode-matching efficiency between scattered and reflected fields. Changes in the

GNR's dielectric environment give rise to a change  $\Delta S$  of the GNR's scattering cross section at the probe wavelength as well as a change in the phase difference between scattered and reflected light  $\Delta(\cos\phi)$  due to the shift of the LSPR frequency. In consequence, the change of detected intensity can be described as  $\Delta P_{PT} \propto \Delta S + \Delta I$ , where

$$\Delta I = \eta(\sqrt{R/S}\cos\phi\Delta S + 2\sqrt{SR}\Delta\cos\phi), \quad (2.2)$$

denotes the change of the interference term. Our setup allows for the adjustment of linear incident (angle:  $\alpha_i$ ) and analyzed (angle  $\alpha_a$ ) polarization as well as of the probe wavelength and, to some extent, of the Gouy phase by adjustment of the GNR's position along the focal axis. We can thus tune  $\cos\phi$  as well as the ratio of  $S/R$  via the projection of the scattered field (polarized along the GNR's long axis) and of the reflected field (incident polarization) on the analyzer axis. We can perform 2D-confocal scans measuring  $\Delta P_{PT}$  and  $P_{det}$  that is scattering and PT signal, simultaneously. Figure. 2.1b presents images of such scans performed for a set of polarization mismatch angles  $\alpha_c = (\alpha_a - \alpha_i)/2$  for crossed ( $\alpha = \alpha_i + \pi/2$ ) and parallel ( $\alpha_a = \alpha_i$ ) configurations of incident versus analyzed polarizations. An example for how  $\Delta P_{PT}$  and  $P_{det}$  scale with  $\alpha_c$  ( $S \gg R$ , 40 nm diameter GNR) is shown in figure. 2.1c. In both cases, we find excellent agreement with the theoretical expected values (fits).

Before discussing the influence of the experimental parameters in detail, we want to demonstrate that the PT signal-to-noise ratio (SNR) indeed correlates with the SNR for analyte detection. To this aim, we compare the PT SNR with the intensity autocorrelation contrast obtained with the same NR in the presence of oil-in-water microemulsion nanodroplets [18]. These nanodroplets simulate the optical properties of  $\approx 250$  kDa proteins without the drawbacks of nonspecific sticking commonly encountered for real protein samples. Prevention of binding conserves the GNR's sensing volume and ensures the comparability of results obtained at different times, while experimental parameters are varied. In the following, we compare PT SNR and autocorrelation contrast for the simplest case of a strongly scattering GNR (i.e.  $S \gg R$ ) with the incident polarization parallel to NR's long axis, the probing wavelength on the red-detuned flank of the LSPR and the NR centered in the focused probe beam. While all other parameters are kept constant, we alter the orientation of the polarization analyzer and observe the changes of the photothermal SNR and of the autocorrelation contrast  $C = G(\tau = 10 \text{ ns})$ . From the latter quantity, we then determine the average perturbation SNR [18] via the following relation:  $SNR_{per} = \sqrt{\frac{C}{1-C}}$

(compare 2.2b). We find that both the autocorrelation contrast (see 2.2a) and the PT-SNR decrease with an increasing difference between  $\alpha_i$  and  $\alpha_a$ . We further find a linear relationship between PT-SNR and  $SNR_{per}$ . This proportionality confirms that PT-spectro-microscopy can indeed be used as a means to probe the response of plasmonic structures for biodetection assays. Here we have made use of the fact that the effective extent of the modulated temperature profile around the nanoparticle depends on the modulation frequency. It scales  $\propto (1/r)e^{-(r-r_{np})/\delta_\tau}$ , where  $\delta_\tau = \sqrt{\frac{D}{\pi\nu}}$  is the thermal attenuation length [79] and  $D$  is the surrounding medium's thermal diffusivity. This means that at low frequencies,  $<100$  kHz, the thermal profile extends beyond the 100 nm range, whereas at  $\approx 100$  MHz, it is confined to a few tens of nanometers around the GNR (compare figure. 2.2d). In turn, the choice of modulation frequency allows us to select how strongly thermal-lens effects, temperature changes in the near field, and the heating of the particle itself contribute to the PT signal. At low frequencies,  $<100$  kHz, thermal-lens effects and near-field effects, as well as thermal changes of the GNR's properties, are probed altogether, whereas for higher frequencies of  $\approx 100$  MHz, only thermal changes occurring in the near field and the particle will be recognized. At still higher frequencies, the response of the particle itself will dominate as the extent and amplitude of the temperature profile diminish further. Microemulsion nanodroplets are only detected in the GNR's near field [18], thus, we have chosen to perform our correlative measurements at a high modulation frequency of 80 MHz. At this frequency,  $\delta_\tau=24$  nm is close to the extent of the near field. The fast modulation therefore allows us to directly reject contributions to the PT signal from outside the GNR's near-field. In order to facilitate this high-frequency modulation, we utilized a fiber-based electro-optic modulator (EOM compare figure. 2.1a) that offers a  $\approx 200$  ps rise time. We now want to better understand the influence of experimental parameters on the PT-SNR. To this aim, we perform PT measurements on NRs with similar aspect ratios but different diameters.

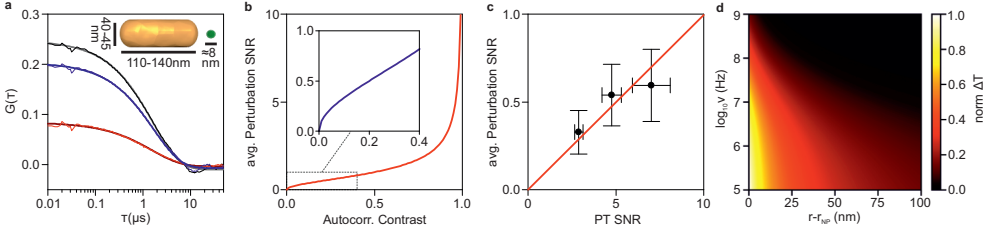


**Figure 2.2:** **a)** Autocorrelations (thin lines) measured in the presence of microemulsion nanodroplets, alongside their respective stretched exponential fits (thick lines). Measurements were obtained on the same GNR with constant incident polarization and different analyzer orientations. The inset shows the dimensions of the sensor GNR and of the nanodroplet (analyte). **b)** The relation between the average perturbation SNR and the autocorrelation contrast. The inset shows the region relevant to the experiment (a). **c)** The measured average perturbation and PT SNRs ( $\nu = 80$  MHz) follow a linear relation (red line: linear fit). **d)** Theoretical values of the temperature amplitude  $\Delta T$  computed as a function of modulation frequency  $\nu$  and of the distance from the surface of a gold sphere with a 20 nm radius.

We first want to discuss the polarization dependence of the PT-signal. While this seems trivial at first, it nonetheless will provide us with insights into the relative strengths of the contributions from  $\Delta S$ ,  $\Delta I$  and  $\Delta \cos\phi$  to  $\Delta P_{det}$ . Specifically, we will focus on the case of parallel incident and analyzed polarizations ( $\alpha_i = \alpha_a$ ). Then, only the scattered field  $E_s$  is angle-dependent and scales like  $E_s(\alpha) = E_s(\alpha = 0)\cos^2\alpha$ , where  $\alpha$  is the angle between the GNR's long axis and the polarizer's orientation. The PT amplitude then scales as:

$$\Delta P_{PT}(\alpha) \propto |\Delta I \cos^2\alpha + \Delta S \cos^4\alpha|, \quad (2.3)$$

where  $\Delta I$  and  $\Delta S$  are the values at  $\alpha = 0$ , and we can determine the relative contribution  $\rho$  of the interference term  $\Delta I$  versus the pure scattering term  $\Delta S$  at  $\alpha = 0$  via fitting to the function:  $\Delta P_{PT}(\alpha) = k|\rho \cos^2\alpha + (1 - |\rho|) \cos^4\alpha|$ , where  $k$  is a constant scaling factor. If we further assume that  $\eta \approx 1$  we can also determine the ratio of intensity changes due to phase shifts over changes of the scattering cross section:

$$\xi = \left| \frac{\rho}{1 - |\rho|} - \sqrt{\frac{R}{S}} \cos\phi \right| = \left| \frac{2\sqrt{SR} \Delta \cos\phi}{\Delta S} \right|, \quad (2.4)$$

Note that  $S/R$  and  $\cos\phi$  are obtained via the simultaneous measurement of the detected power and the subsequent fit to:



$$P_{det}(\alpha)/P_{refl} \propto 1 + 2\sqrt{S/R} \eta \cos\Delta\phi \cos^2\alpha + (S/R) \cos^4\alpha, \quad (2.5)$$

$P_{refl} \propto R$  is measured on the glass slide next to the GNR. The results of our angle-dependent PT measurements are shown in figure. 2.3 alongside the respective values found for  $S/R$ ,  $\cos\phi$ ,  $\rho$  and  $\xi$ . We find that  $\rho$  is negative, which means the interference term counteracts the pure changes in scattered intensity for our confocal configuration. This is especially apparent in figure. 2.3b, which shows the transition from interference- to scattering-dominated PT as  $\alpha$  approaches 0 and results in two minima of PT amplitude. We further find that, as expected for GNRs with  $S/R < 1$ , the interference term significantly contributes to the PT signal ( $|\rho| \geq 0.5$  compare figure. 2.3c,d). Nonetheless, the interference term is still dominated by changes in the scattering cross section ( $\xi < 1$ , figure. 2.3c) as we find that only for GNRs with  $S/R \ll 1$  the phase-shift-induced changes dominate ( $\xi > 1$ , figure. 2.3d). In all cases, we recognize significant PT amplitudes only for polarizations centered around the GNR's long axis. From this we can conclude that we are predominantly probing the GNR's response to temperature changes, and contributions to  $\delta P_{PT}$  due to scattering of light by the thermal lens itself are negligibly small in comparison.

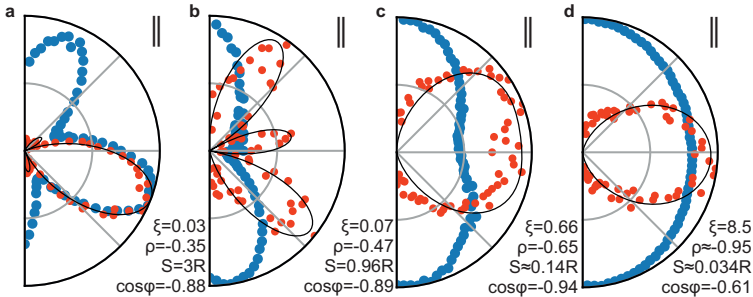


**Figure 2.3:** Parallel-angle scans in (a) to (d) depict the progression from strongly to weakly scattering GNRs showing the transition from scattering- to interference-dominated PT. Black lines are fits of PT amplitude by the respective functions. PT-amplitudes (red dots) and  $P_{det}$  (blue dots) values are normalized to their maximum. All values were measured in water with  $\nu=1.1$  MHz.

We also want to test the wavelength-dependence of the PT signal. To this aim, we first take white-light scattering spectra and determine the GNR's orientation by rotating both polarizers in parallel configuration. We then measure the PT response as we change the wavelength of our laser while keeping the GNR positioned in the center of the focus and both polarizers aligned with the GNR's long axis. Examples

of such measurements performed on three GNRs with different sizes are displayed in figure. 2.4.

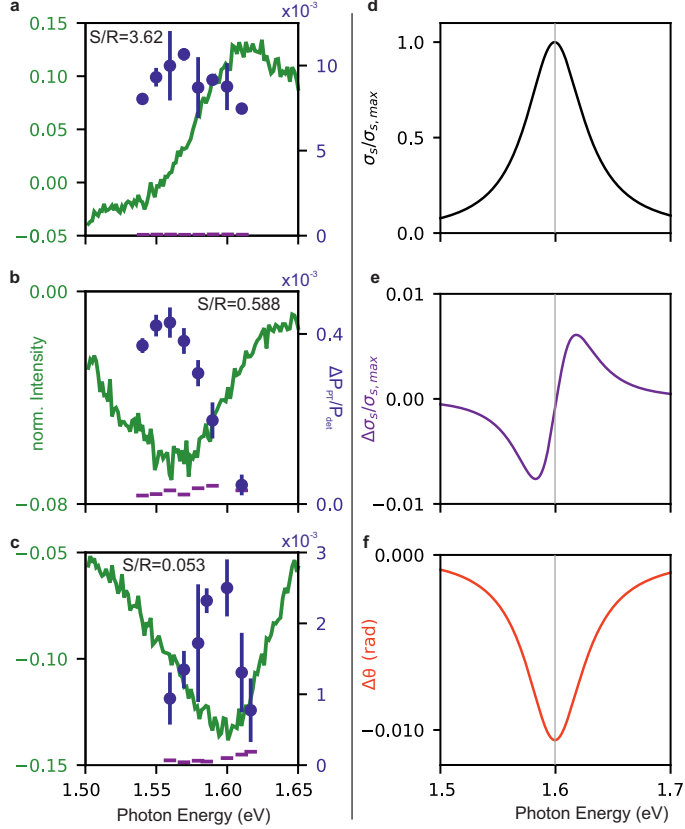


**Figure 2.4:** Left side: Photothermal spectroscopy on GNRs of different sizes (40 to 10 nm diameter) decreasing from (a) to (c). Green lines are normalized white-light scattering spectra. Blue dots are relative intensity changes  $\Delta P_{PT}/P_{det}$  and purple dashes indicate the noise level. Right side: Theoretical curves showing the normalized scattering cross section (d) and its relative change upon a minute reduction of the surrounding medium’s dielectric constant ( $10^{-3}$ ) (e), as well as the associated change of the phase difference between scattered and incident field (f).

We find that the highest relative intensity changes ( $\Delta P_{PT}/P_{det}$ ) for GNR’s with  $S/R > 1$  (figure. 2.4a) coincide with the highest slopes found in the corresponding white-light scattering spectrum. This is consistent with our previous finding that, in the case of  $S/R > 1$ , the PT signal is dominated by changes in the scattered intensity (compare also figure. 2.4e). Due to the limited scanning range of our laser, we unfor-

tunately could not directly compare values on both sides of the LSPR of individual GNRs. For GNRs with  $S/R < 1$  (figure. 2.4b,c) we find the highest  $\Delta P_{PT}/P_{det}$  values close the LSPR frequency. This is consistent with our previous finding that, for GNR's with  $S/R < 1$ , changes in the phase difference  $\phi$  strongly contribute to the PT signal (compare figure. 2.4f).

To obtain an overview of how the PT SNR depends on the GNR size, we plot the maximum  $\Delta P_{PT}/P_{det}$  versus the  $S/R$  values found for multiple GNR samples and normalize these values to the absorbed power (figure. 2.5). The corresponding average refractive index change is computed from the temperature profile [79] in the medium surrounding the rod at distances of up to 15 nm (figure. 2.5b) using the thermorefractive index of water:  $\frac{dn}{dt} = -8.36 \times 10^{-5}(\text{K}^{-1})$ . These values reflect the absorbed power and refractive index sensitivity of the respective GNRs, and we find the highest values  $\Delta P_{PT}/P_{det} = 11.8 \pm 1.6 \text{ RIU}^{-1}$  (refractive index unit) for GNRs with  $S/R \approx 3$  to 5, that is, diameters of approximately 25 nm. This means an effective refractive index change on the order of  $10^3$  gives rise to intensity changes on the order of 1%. For the binding of a single  $\approx 150$  kDa protein, we anticipate relative intensity changes on the same order, that is, 1 to 3%, as found by previous studies [28, 68]. Single step-like changes in relative detected power on the order of 1% are detected by our system with a SNR of  $\approx 1$  at 200 MHz bandwidth. This corresponds to a SNR of  $\approx 4500$  using typical integration times of 100 ms [68]. This yields a detection limit in the range 3 to 9 Da(Hz) $^{-1/2}$  for 0.1 mW of incident power. Our detector is not shot-noise limited and we anticipate an approximately 2-fold improvement of this figure for shot-noise limited detection. We found the maximum refractive index sensitivity for GNRs with diameters of  $\approx 25$  nm. We attribute this finding to the, in comparison to larger GNRs, narrower LSPR of these GNRs (less volume means less radiative damping) and to a still relatively weak contribution from the interference term, which begins to significantly counteract changes in scattering cross section for GNRs with  $S/R \lesssim 1$  (compare figure. 2.3b and figure. 2.4b). This finding, however, has to be taken with caution as this maximum is not only a consequence of the GNR dimensions but also of the experimental conditions and will differ if, for example, a different substrate-medium couple is chosen (with a higher or lower R coefficient). The conditions may be varied further for each individual GNR, for example, by deviating from the parallel polarization configuration we had maintained throughout our measurements in order to compare different GNR sizes.

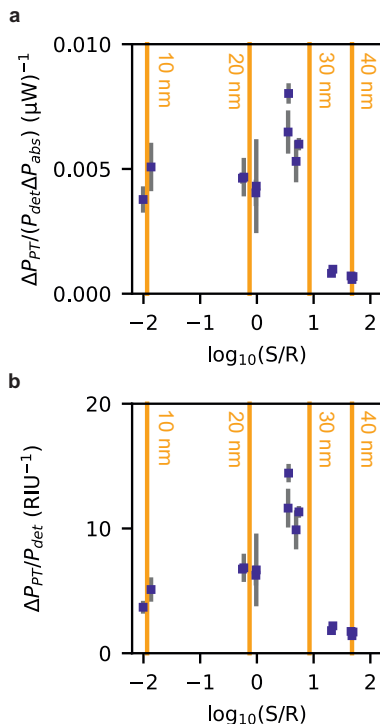


**Figure 2.5:** Comparison of maximum relative PT amplitudes  $\Delta P_{PT}/P_{det}$  found for NRs with different  $S/R$  ratios (diameters indicated in yellow) after optimizing the laser wavelength and aligning the polarizers with the GNR's axis. (a) Measured  $\Delta P_{PT}/P_{det}$  values normalized to the absorbed power and (b)  $\Delta P_{PT}/P_{det}$  normalized to the average change of refractive index units (RIU) calculated for the medium (water) inside the GNR's near field (extent 15 nm).

In fact, variation of polarizers orientation allows almost arbitrarily to set the effective  $S/R$  ratio for any GNR via the projection of the scattered and reflected fields on the GNR, with proper tuning of the analyzer axis. In theory, the highest relative changes  $\Delta P_{PT}/P_{det}$  can be expected for  $S \approx R$ , that is, when  $P_{det}$  approaches zero as a consequence of an almost completely destructive interference between the scattered and reflected fields. This, however, also goes along with a relatively small absolute  $\Delta P_{PT}$ . In turn, whether such a configuration is more desirable will depend on the assay. The desired time resolution for example imposes restrictions on the type of detector that can be used. Here we used a fast avalanche photodiode (APD) in order to detect analytes in Brownian motion with 10 ns temporal resolution (see figure. 2.2a). Whereas this APD has a lower noise-equivalent power than PIN-photodiodes with

similar bandwidth, and is therefore advantageous for our purpose, it suffers from excess noise and is thus not shot-noise limited. In this case setting the polarizers such that  $S = R$  is undesirable as the electronic detector noise already exceeds small signal amplitudes. However, in assays meant to probe slower processes, like analyte binding, singlephoton- counting detectors may be more advantageous. In such a case, the high relative signal amplitudes found at  $S = R$  become desirable as long as the background noise (due to undesired scattering by impurities along the optical path) is still overcome. Independently of an assay's precise nature, PT-assisted alignment may be used to find the most desirable parameters, taking into account the assay's specific restrictions and limitations by available instrumentation.

## 2.4 Conclusion

In conclusion, we have demonstrated that PT-spectromicroscopy can be used as a method for the direct optimization of nanostructure-based optoplasmonic detection assays. Specifically, we have demonstrated this optimization for the case of gold nanorods. We utilized high-frequency modulation to selectively match the thermal modulation profile to the extent of plasmonic near fields. This enabled us to show that the PT SNR scales directly with the SNR found for average perturbations caused by small nanodroplets entering and exiting a NR's near field. We have further demonstrated that PT- micro/spectroscopy helps to probe and understand the influence of various experimental parameters on the SNR. Here, we have specifically identified the best size of GNRs for fast nanoplasmonic assays in a simple confocal bright-field configuration. PT-based calibration uses the refractive index change induced by photothermal heating of the sensor nanostructures themselves and is therefore, in principle, applicable to any type of optoplasmonic assay that probes changes in the dielectric environment of nanostructures.